Journal of Engineering Mathematics **34:** 3–20, 1998.

Low-Reynolds-number flow over partially covered cavities

C. H. DRIESEN, J. G. M. KUERTEN and M. STRENG
Faculty of Applied Mathematics, University of Twente, P.O. Box 217, 7500 AE Enschede, The Netherlands

Received 19 September 1996; accepted in revised form 17 June 1997

Abstract. We solve the problem of two-dimensional flow of a viscous fluid over a rectangular approximation of an etched hole. In the absence of inertia, the problem is solved by a technique involving the matching of biorthogonal infinite eigenfunction expansions in different parts of the domain. Truncated versions of these series are used to compute a finite number of unknown coefficients. In this way, the stream function and its derivatives can be determined in any arbitrary point. The accuracy of the results and the influence of the singularities at the mask-edge corners is discussed. The singularities result in a reduced convergence of the eigenfunction expansions on the interfaces of the different regions. However, accurate results can be computed for the interior points without using a lot of computational time and memory. These results can be used as a benchmark for other methods which will have to be used for geometries involving curved boundaries. The effect of hole size on the flow pattern is also discussed. These flow patterns have a strong influence on the etch rate in the different regions.

Key words: creeping flow, cavity, etching, biorthogonal series, masks.

1. Introduction

The mathematical modelling of flows over open cavities has been a topic of research for at least three decades. These investigations are often concerned with the transport of heat or mass from the cavity to the flow outside or, alternatively, from the outer flow to the cavity walls. Some early examples are [1, 2, 3, 4, 5].

In wet-chemical etching a special variety of this problem emerges, namely that of the flow past a partially covered cavity (Figure 1). In etching, a fluid containing aggressive chemicals, the etchant, is brought into contact with a solid that is to be etched. Often, the purpose of the etching process is to dissolve only certain parts of the solid, so that holes, trenches or grooves are produced. To achieve the required result, the solid is covered with a layer of non-etchable material which is called the mask or photo-resist. The etchant is then allowed to dissolve the solid through the holes left in the mask. Since sideways etching and etching in depth are phenomena which occur simultaneously, a shape such as that depicted in Figure 1 can be expected to result from a process of this kind.

In etching we are usually concerned with very small holes, downwards from about 100 microns. Since flow velocities within such small holes can never be very large and will decrease with hole size, these flows are most likely of the low-Reynolds-number kind. On the other hand, the diffusion coefficients of species dissolved in the fluid, *i.e.* in the case of wet-chemical etching, are smaller than the kinematic viscosity by a factor which is typically of the order of 10^4–10^5. Therefore, in spite of the creeping-flow character of the flow, the transport of dissolved species can still be convection-dominated, even for very small holes.

Kuiken [6] and Kuiken and Tijburg [7] showed that the nature of the flow inside the cavity strongly determines the etch rates. It is the trapped-eddy structure which wholly determines the etching process. In [6] a model involving interconnecting convection-diffusion boundary layers was developed for such processes. Using Levêque-type approximations and invoking

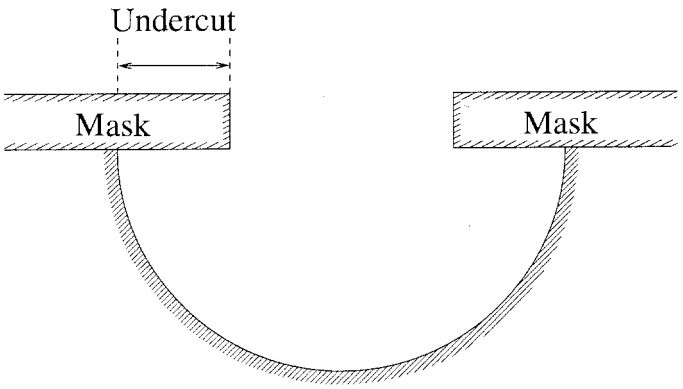

Figure 1. Etch hole with undercut.

transformations of a kind pioneered by Lighthill [8], the author of [6] was able to derive a set of coupled integral equations, with all the information about the flow field hidden in the transformed variables.

Since, in the case of forced flow, the flow is not influenced by the spatial distribution of the dissolved species, except perhaps through a weak concentration dependence of the viscosity that we shall disregard here, one first step towards the understanding of convection-assisted etching will be to describe the flow within a complicated geometry of a kind as shown in Figure 1. A full description of the etching process will involve a succession of such shapes, each of which follows from the flow field in a quasi-stationary manner, whereby the above-mentioned system of integral equations provides the link towards the moving-boundary condition.

In this paper we shall be solely concerned with the fluid-flow aspects of problems of the afore-mentioned kind. Since an accurate numerical simulation of fluid flows in a complicated geometry such as that of Figure 1 is by no means simple, it is useful to consider different methods and slightly modified geometries for this problem. In a series of papers on slow viscous flow Joseph and coworkers [9, 10, 11] showed that accurate semi-analytical solutions can be obtained for geometries involving straight edges only. They used a method involving biorthogonal series expansions. In particular. Trogdon and Joseph [12] consider a geometry which corresponds to Figure 2 with f equal to zero.

Clearly, the difference between the geometry considered by Trogdon and Joseph and the geometry considered here is the presence of the overhanging mask edges. In this paper we derive solutions for flows inside the rectangular cavity of Figure 2 and driven by a uniform-shear flow outside. We study the influence of the singularities on the mask-edge corners with respect to the accuracy of the solution. We also study the influence of the number of terms included in the biorthogonal series solutions on the accuracy.

Recently, mass transport in multiple-eddy systems has been a subject of intense research, particularly in the context of etching. In a series of papers [13, 14, 15] Alkire and coworkers considered various aspects of this problem in both rectangular and circular cut-outs. These studies give insight into the nature of the flow inside these cut-outs and in the mass-transport properties of such systems in the absence of masks. Alkire *et al.* recognise the boundary-layer character of mass transport and apply a method of the kind first put forward in [6] in their mathematical model.

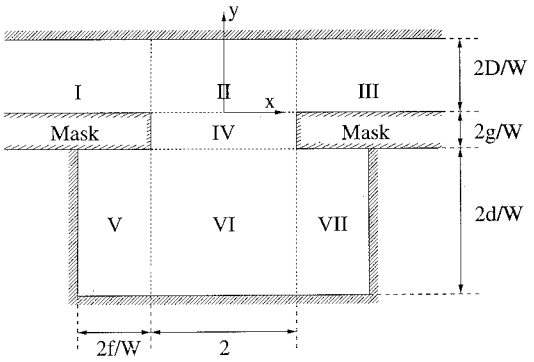

Figure 2. Geometry and definition of parameters and subregions.

Shin and Economou [16, 17] employ a finite-element calculation to simulate the shape evolution of cavities in the presence of thick masks. They consider both forced and natural convection. Their paper is rich in graphical material. However, their method does not exploit the boundary-layer character of mass transport. Other papers which are of interest in this context are [18] and [19]. The first considers flow and convection in triangular trenches and uses a finite-element package, while the second focusses on convection-diffusion in rectangular slots and employs a combination of boundary and spectral elements to arrive at an accurate solution. Again, masks are absent in these studies.

Thus, the purpose of this paper is to provide solutions for creeping flows over and inside partially covered cavities by means of biorthogonal eigenfunction expansions. We consider the accuracy of our computations, and relate this to the singularities at the mask-edge corners. Other methods of solution, *e.g.* boundary-element or finite-element methods, which will have to be used in more general cases involving curved boundaries, can be compared with these solutions. In order to facilitate such comparisons, we shall list a series of pertinent results for future reference.

In the next section, we give the mathematical formulation of the fluid-flow problem. In Section 3 we show how the flow domain is subdivided into a finite number of rectangular sub-domains. In each of these sub-domains the solution is then formulated formally in terms of a biorthogonal series expansion [9, 10, 11]. These formulations contain coefficients which can be fully determined by the boundary conditions (Section 4) and matching conditions (Section 5). With the help of biorthogonal functions a linear system for the coefficients is constructed in Section 6. The accuracy of our calculations is described in Section 7, and some results are shown in Section 8.

2. Mathematical formulation

We consider the two-dimensional geometry as shown in Figure 2. We compute the flow inside a rectangular etched hole resulting from the moving upper plate. This upper plate is needed for our solution method, but, clearly, a uniform shear flow can be simulated with such a plate. We apply the incompressible Navier–Stokes equations to our physical domain. These equations are scaled by the model parameters and the inertial terms are neglected on account of the Reynolds number being small. The resulting equations are

$$-\nabla p + \mu \nabla^2 \boldsymbol{u} = 0 \tag{2.1}$$

and the continuity equation is

$$\nabla \cdot \boldsymbol{u} = 0. \tag{2.2}$$

Here p denotes the pressure, $\boldsymbol{u}$ the velocity vector and μ the kinematic viscosity. Taking the curl of (2.1) we can rewrite the equations as a single biharmonic equation

$$\nabla^4 \Psi = 0, \tag{2.3}$$

where the stream function Ψ is defined as

$$u = \frac{\partial \Psi}{\partial y}, \qquad v = -\frac{\partial \Psi}{\partial x},$$

where u and v are the velocities in x and y direction respectively. The boundary conditions

$$\frac{\partial \Psi}{\partial n} = 0 \quad \text{and} \quad \Psi = \text{constant}, \tag{2.4}$$

describe the no-slip condition on the walls, the constant being equal to a positive value on the moving plate and zero elsewhere. The hole sizes are defined in Figure 2, where all parameters are scaled with the semi-width of the inlet W. This scaling parameter is chosen because, during etching, it remains the same.

Solutions of (2.3) are the so-called Papkovich–Fadle eigenfunctions [20, 21]. These eigenfunctions arise from separation of variables in a natural way. In the next section we describe how the solution of our problem can be formulated in terms of these eigenfunctions.

3. Solution procedure

The flow domain is divided into seven subregions as shown in Figure 2. For each of these regions boundary conditions can be used to reduce the number of unknown coefficients in the eigenfunction expansions. For each subregion the resulting series of eigenfunctions are given below. In the next sections the remaining boundary conditions are used, together with matching conditions for the region interfaces, to compute the unknown coefficients. After an integration procedure described in Section 6, this results in a linear system of equations for the coefficients.

The only remaining problem is that each series contains an infinite number of coefficients. Therefore, we truncate the series, which leads to a finite number of linear equations for the unknown coefficients.

As described above, we first give the series of eigenfunctions for each subregion. For the second region, the solution takes the form

$$\begin{aligned}\Psi^{\mathrm{II}}(x,y) \;=\; & f(y) + \sum_{k=-\infty}^{\infty} \frac{Q_k}{\widehat{P}_k^2}\widehat{\phi}_k(y)\frac{\cosh \widehat{P}_k x}{\cosh \widehat{P}_k} + \sum_{k=-\infty}^{\infty} \frac{Q_k^*}{\widehat{P}_k^{*2}}\widehat{\phi}_k^*(y)\frac{\cosh \widehat{P}_k^* x}{\cosh \widehat{P}_k^*} \\ & + \sum_{k=-\infty}^{\infty} \frac{A_k}{P_k^2}\phi_k(x)\frac{\sinh P_k(y - D/W)}{\sinh P_k D/W} \\ & + \sum_{k=-\infty}^{\infty} \frac{B_k}{P_k^2}\phi_k(x)\frac{\cosh P_k(y - D/W)}{\cosh P_k D/W},\end{aligned} \tag{3.1}$$

where

$$\phi_k(x) = P_k[\sin P_k \cos P_k x - x \cos P_k \sin P_k x] \tag{3.2}$$

and

$$\begin{aligned}\widehat{\phi}_k(y) \;=\; P_k \Bigg[&\sin P_k \cos P_k \left(\frac{y - D/W}{D/W}\right) \\ &- \left(\frac{y - D/W}{D/W}\right) \cos P_k \sin P_k \left(\frac{y - D/W}{D/W}\right)\Bigg].\end{aligned} \tag{3.3}$$

Here, for $k > 0$, the P_k are the first-quadrant complex roots of

$$\sin 2P_k + 2P_k = 0, |P_1| < |P_2| < \cdots < |P_k|, P_{-k} = \overline{P}_k.$$

Further

$$\begin{aligned}\widehat{\phi}^*_k(y) \;=\; P^*_k \Bigg[&\cos P^*_k \sin P^*_k \left(\frac{y - D/W}{D/W}\right) \\ &- \left(\frac{y - D/W}{D/W}\right) \sin P^*_k \cos P^*_k \left(\frac{y - D/W}{D/W}\right)\Bigg],\end{aligned} \tag{3.4}$$

where, for $k > 0$, the P^*_k are the first-quadrant complex roots of

$$\sin 2P^*_k - 2P^*_k = 0, \quad |P^*_1| < |P^*_2| < \cdots < |P^*_k|, \quad P^*_{-k} = \overline{P}^*_k.$$

Also

$$f(y) = \tfrac{1}{4}y^2.$$

The function $f(y)$ is the Couette-part of the stream function as caused by the moving upper plate in the absence of the hole. Robbins and Smith [22] explain how the values of P_k and P^*_k can be computed. The solution in region I must be matched with the solution in region II on the line $x = -1$. In region I the solution takes the form

$$\Psi^{\mathrm{I}}(x, y) = f(y) + \sum_{k=-\infty}^{\infty} \frac{C_k}{\widehat{P}_k^2} \widehat{\phi}_k(y)\, \mathrm{e}^{\widehat{P}_k(x+1)} + \sum_{k=-\infty}^{\infty} \frac{C^*_k}{\widehat{P}_k^{*2}} \widehat{\phi}^*_k(y)\, \mathrm{e}^{\widehat{P}^*_k(x+1)}. \tag{3.5}$$

The solution in region III is the mirror image of the solution in region I

$$\Psi^{\mathrm{III}}(x, y) = \Psi^{\mathrm{I}}(-x, y). \tag{3.6}$$

These solutions satisfy the boundary conditions on the upper plate and on the upper mask edges. For the other regions, the solutions are given in the order of the region numbers: In region IV the solution is given by

$$\begin{aligned}\Psi^{\mathrm{IV}}(x, y) \;=\; &\sum_{k=-\infty}^{\infty} \frac{Y_k}{P_k^2} \phi_k(x) \frac{\sinh P_k(-(y + g/W))}{\sinh P_k g/W} \\ &+ \sum_{k=-\infty}^{\infty} \frac{Z_k}{P_k^2} \phi_k(x) \frac{\cosh P_k(-(y + g/W))}{\cosh P_k g/W}.\end{aligned} \tag{3.7}$$

Region V

$$\begin{aligned}\Psi^{\mathrm{V}}(x,y) \;=\; & \sum_{k=-\infty}^{\infty} \frac{T_k}{\widetilde{P}_k^2}\widetilde{\phi}_k(y)\frac{\cosh \widetilde{P}_k(x+1+f/W)}{\cosh \widetilde{P}_k f/W} \\ & + \sum_{k=-\infty}^{\infty} \frac{V_k}{\widetilde{P}_k^2}\widetilde{\phi}_k(y)\frac{\sinh \widetilde{P}_k(x+1+f/W)}{\sinh \widetilde{P}_k f/W} \\ & + \sum_{k=-\infty}^{\infty} \frac{T_k^*}{\widetilde{P}_k^{*2}}\widetilde{\phi}_k^*(y)\frac{\cosh \widetilde{P}_k^*(x+1+f/W)}{\cosh \widetilde{P}_k^* f/W} \\ & + \sum_{k=-\infty}^{\infty} \frac{V_k^*}{\widetilde{P}_k^{*2}}\widetilde{\phi}_k^*(y)\frac{\sinh \widetilde{P}_k^*(x+1+f/W)}{\sinh \widetilde{P}_k^* f/W}. \end{aligned} \tag{3.8}$$

The solution in region VII is the mirror image of the solution in region V

$$\Psi^{\mathrm{VII}}(x,y) = \Psi^{\mathrm{V}}(-x,y). \tag{3.9}$$

Region VI

$$\begin{aligned}\Psi^{\mathrm{VI}}(x,y) \;=\; & \sum_{k=-\infty}^{\infty} \frac{S_k}{\widetilde{P}_k^2}\widetilde{\phi}_k(y)\frac{\cosh \widetilde{P}_k x}{\cosh \widetilde{P}_k} \\ & + \sum_{k=-\infty}^{\infty} \frac{S_k^*}{\widetilde{P}_k^{*2}}\widetilde{\phi}_k^*(y)\frac{\cosh \widetilde{P}_k^* x}{\cosh \widetilde{P}_k^*} \\ & + \sum_{k=-\infty}^{\infty} \frac{D_k}{P_k^2}\phi_k(x)\frac{\sinh P_k(-(y+2g/W+d/W))}{\sinh P_k d/W} \\ & + \sum_{k=-\infty}^{\infty} \frac{E_k}{P_k^2}\phi_k(x)\frac{\cosh P_k(-(y+2g/W+d/W))}{\cosh P_k d/W}. \end{aligned} \tag{3.10}$$

In these formulas, the functions $\widetilde{\phi}_k(y)$ and $\widetilde{\phi}_k^*(y)$ are given by

$$\widetilde{\phi}_k(y) = \phi_k\left(\frac{-(y+2g/W+d/W)}{d/W}\right), \quad \text{and} \quad \widetilde{\phi}_k^*(y) = \phi_k^*\left(\frac{-(y+2g/W+d/W)}{d/W}\right)$$

and thus

$$\widehat{P}_k = \frac{P_k}{D/W}, \quad \widehat{P}_k^* = \frac{P_k^*}{D/W}, \quad \widetilde{P}_k = \frac{P_k}{d/W}, \quad \widetilde{P}_k^* = \frac{P_k^*}{d/W}. \tag{3.11}$$

By substituting solutions (3.1), (3.5), (3.7), (3.8) and (3.10) in (2.3) we may verify that the given solutions are biharmonic. Summarising, we have derived for each subregion a number of infinite series of unknown coefficients, using the general solutions of the biharmonic equation and some of the boundary conditions. In the next section, the remaining boundary conditions

are used to derive relations between the coefficients. In Section 5, the matching conditions will be used to complete the system of equations.

4. Boundary conditions

Now, we show how the remaining boundary conditions are used to formulate relations between the unknown coefficients. As an example of such a boundary condition, we consider the series for the second region. For this region, (3.1) must satisfy the boundary conditions on the upper (moving) plate

$$\Psi^{\mathrm{II}}(x, 2D/W) = f(2D/W) \tag{4.1}$$

and

$$\frac{\partial \Psi^{\mathrm{II}}}{\partial y}(x, 2D/W) = f'(2D/W). \tag{4.2}$$

Substitution of (3.1) in (4.1) and (4.2) gives the following conditions for the coefficients A_k and B_k

$$\sum_{k=-\infty}^{\infty} [A_k + B_k] \frac{\phi_k(x)}{P_k^2} = 0 \tag{4.3}$$

and

$$\sum_{k=-\infty}^{\infty} [A_k + B_k] \phi_k(x) + \sum_{k=-\infty}^{\infty} \left[A_k \left(\frac{\coth P_k D/W - P_k}{P_k} \right) + B_k \left(\frac{\tanh P_k D/W - P_k}{P_k} \right) \right] \phi_k(x) = 0. \tag{4.4}$$

In the same way, boundary conditions in region V and region VI can be derived.

In the next section, we show how the matching conditions on the region interfaces lead to additional relations between the unknown coefficients. From the resulting set of equations, the coefficients can be completely determined.

5. Matching conditions

We require the continuity of velocities and stresses across common boundaries between the subregions. It is not hard to show that the velocities and stresses are continuous across the boundary if the stream functions on the left (Ψ^L) and right (Ψ^R) side of this boundary satisfy

$$\Psi^L = \Psi^R, \quad \frac{\partial \Psi^L}{\partial n} = \frac{\partial \Psi^R}{\partial n}, \quad \frac{\partial^2 \Psi^L}{\partial n^2} = \frac{\partial^2 \Psi^R}{\partial n^2}, \quad \frac{\partial^3 \Psi^L}{\partial n^3} = \frac{\partial^3 \Psi^R}{\partial n^3}. \tag{5.1}$$

We take the region interface between region I and region II as an example. Substitution of (3.5) and (3.1) in (5.1) leads to the following relations between the coefficients of the series in these regions. For the continuity of the stream function this gives

$$\sum_{k=-\infty}^{\infty} [C_k - Q_k] \frac{\widehat{\phi}_k(y)}{\widehat{P}_k^2} + \sum_{k=-\infty}^{\infty} [C_k^* - Q_k^*] \frac{\widehat{\phi}_k^*(y)}{\widehat{P}_k^{*2}} = 0. \tag{5.2}$$

For the first derivatives, this results in

$$\sum_{k=-\infty}^{\infty} \widehat{P}_k[C_k + Q_k \tanh \widehat{P}_k] \frac{\widehat{\phi}_k(y)}{\widehat{P}_k^2} + \sum_{k=-\infty}^{\infty} \widehat{P}_k^*[C_k^* + Q_k^* \tanh \widehat{P}_k^*] \frac{\widehat{\phi}_k^*(y)}{\widehat{P}_k^{*2}} = 0. \tag{5.3}$$

The equation for the second derivatives becomes

$$\begin{aligned} &\sum_{k=-\infty}^{\infty} [C_k - Q_k] \widehat{\phi}_k(y) + \sum_{k=-\infty}^{\infty} [C_k^* - Q_k^*] \widehat{\phi}_k^*(y) \\ &\quad = \sum_{k=-\infty}^{\infty} \frac{B_k}{P_k^2} \phi_k''(1) \frac{\cosh P_k(y - D/W)}{\cosh P_k D/W} + \sum_{k=-\infty}^{\infty} \frac{A_k}{P_k^2} \phi_k''(1) \frac{\sinh P_k(y - D/W)}{\sinh P_k D/W}. \end{aligned} \tag{5.4}$$

For the third derivatives we can derive the following equation

$$\begin{aligned} &\sum_{k=-\infty}^{\infty} \widehat{P}_k[C_k + Q_k \tanh \widehat{P}_k] \widehat{\phi}_k(y) + \sum_{k=-\infty}^{\infty} \widehat{P}_k^*[C_k^* + Q_k^* \tanh \widehat{P}_k^*] \widehat{\phi}_k^*(y) \\ &\quad = - \sum_{k=-\infty}^{\infty} \frac{B_k}{P_k^2} \phi_k'''(1) \frac{\cosh P_k(y - D/W)}{\cosh P_k D/W} \\ &\qquad - \sum_{k=-\infty}^{\infty} \frac{A_k}{P_k^2} \phi_k'''(1) \frac{\sinh P_k(y - D/W)}{\sinh P_k D/W}. \end{aligned} \tag{5.5}$$

In the same way, the matching conditions for the other interfaces can be derived. The resulting equations contain the unknown series of coefficients, and are functions of one variable along each of the interfaces. In the next section this last dependence is removed in the following way. First, the equations are rewritten in a vector form. Subsequently, a biorthogonal integration method is applied to these modified equations.

6. Biorthogonality

In the previous section, all matching conditions were used to derive a set of equations, from which the unknown infinite series of coefficients can completely be determined. However, each of the foregoing equations represents the expansion of a function of one variable in different sets of eigenfunctions. By using biorthogonality properties of these eigenfunctions, we can simplify the relations.

To this end the equations are expressed in a vector form which will facilitate the implementation of biorthogonality. Following our examples of the previous section, we give the definitions to reformulate the problems vectorial form. We define the vectors [12]

$$\begin{aligned} &\phi_1^k(s) = \phi_k(s), \quad \phi_2^k(s) = \phi_k''(s)/P_k^2, \\ &\widehat{\phi}_1^k(s) = \widehat{\phi}_k(s), \quad \widehat{\phi}_2^k(s) = \widehat{\phi}_k''(s)/\widehat{P}_k^2, \\ &\widehat{\phi}_1^{*k}(s) = \widehat{\phi}_k^*(s), \quad \widehat{\phi}_2^{*k}(s) = \widehat{\phi}_k^{*\prime\prime}(s)/\widehat{P}_k^{*2}. \end{aligned}$$

Similar vectors can be defined for the other series expansions. With these vectors, the equations can be transformed into vector forms. For the example (4.3) and (4.4) the vector

form becomes

$$\sum_{k=-\infty}^{\infty}[A_k+B_k]\begin{bmatrix}\phi_1^k(x)\\ \phi_2^k(x)\end{bmatrix}+\sum_{k=-\infty}^{\infty}\left[A_k\left(\frac{\coth P_kD/W-P_k}{P_k}\right)\right.$$

$$\left.+B_k\left(\frac{\tanh P_kD/W-P_k}{P_k}\right)\right]\begin{bmatrix}\phi_1^k(x)\\ 0\end{bmatrix}=\begin{bmatrix}0\\ 0\end{bmatrix}. \tag{6.1}$$

For (5.2) and (5.4) the vector form is written as

$$\sum_{k=-\infty}^{\infty}[C_k-Q_k]\begin{bmatrix}\widehat{\phi}_1^k(y)\\ \widehat{\phi}_2^k(y)\end{bmatrix}+\sum_{k=-\infty}^{\infty}[C_k^*-Q_k^*]\begin{bmatrix}\widehat{\phi}_1^{*k}(y)\\ \widehat{\phi}_2^{*k}(y)\end{bmatrix}$$

$$=\begin{bmatrix}\displaystyle\sum_{k=-\infty}^{\infty}\frac{B_k}{P_k^2}\phi_k''(1)\frac{\cosh P_k(y-D/W)}{\cosh P_kD/W}\\ 0\end{bmatrix}$$

$$+\begin{bmatrix}\displaystyle\sum_{k=-\infty}^{\infty}\frac{A_k}{P_k^2}\phi_k''(1)\frac{\sinh P_k(y-D/W)}{\sinh P_kD/W}\\ 0\end{bmatrix}. \tag{6.2}$$

For (5.3) and (5.5)

$$\sum_{k=-\infty}^{\infty}\widehat{P}_k[C_k-Q_k\tanh\widehat{P}_k]\begin{bmatrix}\widehat{\phi}_1^k(y)\\ \widehat{\phi}_2^k(y)\end{bmatrix}+\sum_{k=-\infty}^{\infty}\widehat{P}_k^*[C_k^*+Q_k^*\tanh\widehat{P}_k^*]\begin{bmatrix}\widehat{\phi}_1^{*k}(y)\\ \widehat{\phi}_2^{*k}(y)\end{bmatrix}$$

$$=-\begin{bmatrix}\displaystyle\sum_{k=-\infty}^{\infty}\frac{B_k}{P_k^2}\phi_k'''(1)\frac{\cosh P_k(y-D/W)}{\cosh P_kD/W}\\ 0\end{bmatrix}$$

$$-\begin{bmatrix}\displaystyle\sum_{k=-\infty}^{\infty}\frac{A_k}{P_k^2}\phi_k'''(1)\frac{\sinh P_k(y-D/W)}{\sinh P_kD/W}\\ 0\end{bmatrix}. \tag{6.3}$$

To obtain the expressions above we differentiated (4.3), (5.2) and (5.4) twice. For the other matching and boundary conditions a similar procedure is followed. The biorthogonality properties for the eigenfunctions appearing in (6.1) to (6.3) are summarised below. These properties are derived by Smith in [23]

$$\int_{-1}^{1}\boldsymbol{A}\boldsymbol{\phi}^k(s)\cdot\boldsymbol{\psi}^n(s)\,\mathrm{d}s=k_n\delta_{nk},$$

$$\int_0^{2D/W}\boldsymbol{A}\widehat{\boldsymbol{\phi}}^k(s)\cdot\widehat{\boldsymbol{\psi}}^n(s)\,\mathrm{d}s=k_nD/W\delta_{nk},$$

$$\int_0^{2D/W}\boldsymbol{A}\widehat{\boldsymbol{\phi}}^{*k}(s)\cdot\widehat{\boldsymbol{\psi}}^{*n}(s)\,\mathrm{d}s=k_n^*D/W\delta_{nk},$$

where

$$\boldsymbol{A} = \begin{bmatrix} 0 & -1 \\ 1 & 2 \end{bmatrix},$$
$$k_n = -4\cos^4 P_n,$$
$$k_n^* = -4\sin^4 P_n^*,$$
$$\boldsymbol{\phi}^k(s) = \begin{bmatrix} \phi_1^k(s) \\ \phi_2^k(s) \end{bmatrix}$$

and $\boldsymbol{\psi}^n(s)$ and $\boldsymbol{\psi}^{*n}(s)$ are the vectors containing the even and odd adjoint eigenfunctions, respectively. The adjoint eigenfunctions are given by Joseph and Sturges [10] as

$$\psi_1^n(s) = \phi_1^n(s) - 2\cos P_n \cos P_n s = \psi_n(s), \quad \psi_2^n(s) = -\frac{\psi_n''(s)}{P_n^2} = \phi_1^n(s),$$
$$\psi_1^{*n}(s) = \phi_1^{*n}(s) + 2\sin P_n^* \sin P_n^* s = \psi_n^*(s), \quad \psi_2^{*n}(s) = -\frac{\psi_n^{*\prime\prime}(s)}{P_n^{*2}} = \phi_1^{*n}(s).$$

The adjoint eigenfunctions, $\widehat{\boldsymbol{\psi}}^n(s), \widehat{\boldsymbol{\psi}}^{*n}(s)$ bear the same relationship to $\widehat{\boldsymbol{\phi}}^n(s)$ and $\widehat{\boldsymbol{\phi}}^{*n}(s)$ as $\boldsymbol{\psi}^n(s)$ and $\boldsymbol{\psi}^{*n}(s)$ do to $\boldsymbol{\phi}^n(s)$ and $\boldsymbol{\phi}^{*n}(s)$. To implement biorthogonality, we use the operators defined below

$$\int_{-1}^{1} \boldsymbol{A}(\circ) \cdot \boldsymbol{\psi}^n(s)\,\mathrm{d}s, \tag{6.4}$$

$$\int_{0}^{2D/W} \boldsymbol{A}(\circ) \cdot \widehat{\boldsymbol{\psi}}^n(s)\,\mathrm{d}s, \tag{6.5}$$

$$\int_{0}^{2D/W} \boldsymbol{A}(\circ) \cdot \widehat{\boldsymbol{\psi}}^{*n}(s)\,\mathrm{d}s. \tag{6.6}$$

The same kind of operator can be defined for the other basic functions. These operators are applied to the vector equations. As an example, the following results can be obtained. The operator (6.5) is applied to (6.2) and (6.3). This results in

$$C_n - Q_n = \sum_{k=-\infty}^{\infty} \frac{B_k}{k_n P_k^2} \phi_k''(1) \Lambda(\widehat{P}_n, P_k) \tag{6.7}$$

and

$$C_n + Q_n \tanh \widehat{P}_n = -\sum_{k=-\infty}^{\infty} \frac{B_k}{k_n P_k^2 \widehat{P}_n} \phi_k'''(1) \Lambda(\widehat{P}_n, P_k), \tag{6.8}$$

where

$$\Lambda(\widehat{P}_n, P_k) = \frac{1}{\cosh P_k D/W} \int_0^{2D/W} \cosh P_k(y - D/W) \widehat{\psi}_2^n(y)\,\mathrm{d}y.$$

The operator (6.6) is applied to the same linear equations, which results in

$$C_n^* - Q_n^* = \sum_{k=-\infty}^{\infty} \frac{A_k}{k_n^* P_k^2} \phi_k''(1) \Lambda^*(\widehat{P}_n^*, P_k) \tag{6.9}$$

and

$$C_n^* + Q_n^* \tanh \widehat{P}_n^* = - \sum_{k=-\infty}^{\infty} \frac{A_k}{k_n^* P_k^2 \widehat{P}_n^*} \phi_k'''(1) \Lambda^*(\widehat{P}_n^*, P_k), \tag{6.10}$$

where

$$\Lambda^*(\widehat{P}_n^*, P_k) = \frac{1}{\sinh P_k D/W} \int_0^{2D/W} \sinh P_k (y - D/W) \widehat{\psi}_2^{*n}(y) \, \mathrm{d}y.$$

Next the operator (6.4) is applied to (6.1), which results in

$$A_n + B_n + \sum_{k=-\infty}^{\infty} A_k \left(\frac{\coth P_k D/W - P_k}{P_k} \right) \frac{G_{nk}}{k_n} + \sum_{k=-\infty}^{\infty} B_k \left(\frac{\tanh P_k D/W - P_k}{P_k} \right) \frac{G_{nk}}{k_n} = 0, \tag{6.11}$$

where

$$G_{nk} = \int_{-1}^{1} \psi_2^n(x) \phi_1^k(x) \, \mathrm{d}x.$$

In the same way as presented above, 16 linear systems can be derived for the 16 unknown series of coefficients. To solve these equations, these systems have to be truncated. The remaining linear systems of equations are solved by substitution. In the next section, the accuracy of the computations is discussed. Some results are presented in Section 8.

7. Accuracy

Before presenting the results in the next section, we first discuss the two main sources of error in our computations.

From the series, the second derivative normal to an arbitrary interface can be computed. However, the series for this derivative converge only slowly on the region interface. Using extrapolation from the interior of a region, we can compute the second derivative more accurately from a small number of terms. The series on both sides of the interface result in two values for each interface point, which differ in the order of 10 percent. It should be noted that these discontinuities are not in contradiction with the matching conditions, since the matching conditions are not fulfilled point-wise but only in a global sense. The discontinuities are caused by the singularities at the mask-edge corners. The behaviour of such a singularity is shown in Figure 3, where the vorticity around a mask-edge corner is plotted. As we will show, the convergence behaviour of the series of coefficients is determined by these singularities. The singular behaviour near the mask-edge corners is computed with the procedure described by

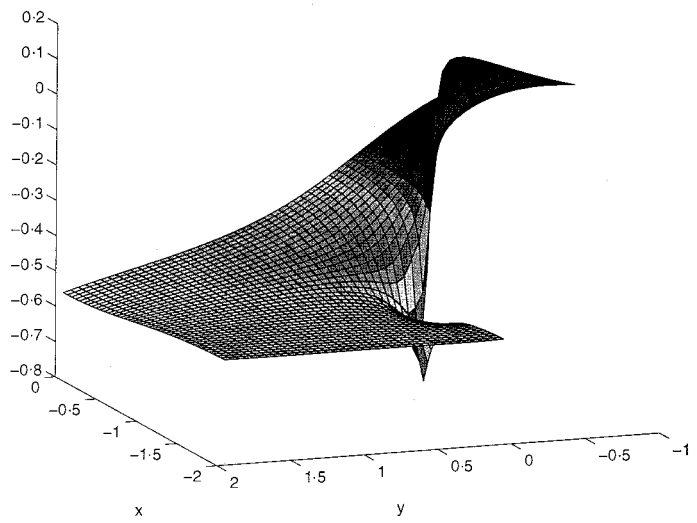

Figure 3. The vorticity $\partial v/\partial x - \partial u/\partial y$ plotted around a mask-edge corner.

Moffatt [24]. In this procedure a solution is computed for the biharmonic equation in plane polar co-ordinates (r, θ) of the form

$$\Psi = r^{\lambda} f_{\lambda}(\theta), \tag{7.1}$$

where λ is any number, real or complex, which may be called the exponent of the solution. This solution is computed for the flow around the mask-edge corners, which gives for the first values for the exponent λ

$$\begin{aligned} \lambda_1 &\simeq 1{\cdot}54448 & \lambda_4 &\simeq 3{\cdot}30133 + 0{\cdot}31584i, \\ \lambda_2 &\simeq 1{\cdot}90853 & \lambda_5 &\simeq 3{\cdot}97184 + 0{\cdot}37393i, \\ \lambda_3 &\simeq 2{\cdot}62926 + 0{\cdot}23125i & \lambda_6 &\simeq 4{\cdot}64142 + 0{\cdot}41879i. \end{aligned}$$

The smallest value describes the asymptotic behaviour at the corners. With the first three exponents a function is constructed along the first region interface, which is the interface between region I and II. The function is constructed in such a way that it also satisfies the boundary conditions. This function is expanded in a series of the form (3.5). The convergence of the coefficients of this series shows the same behaviour as we found in our computations for the biharmonic problem.

These calculations give rise to doubts about the quality of the method, since the discontinuous second derivatives were used to construct the matching conditions for the computation of the unknown coefficients. Similar problems were found in a computation with a matching problem for the Laplace equation, where the first derivative showed discontinuities at the region interfaces [25]. However, since for the Laplace problem the analytical solution was known, it could also be shown, that the solution in the interior can be computed with any desired accuracy. In [26] similar problems appeared in a driven cavity, where the biharmonic problem was solved by a spectral multigrid method. For the interior points, an accurate solution was computed, while the accuracy of the computations decreased near the boundaries.

Table 1. Convergence behaviour of velocities at arbitrary points as a function of the truncation number N. See Figure 4 for definition of the points.

	Point 1	Point 2	Point 3	Point 4	Point 5
x	−1·5	0·5	−0·5	−2·5	−1·0
y	0·5	1·5	−1·5	−2·5	−3·5
N	u $(10^{-1}$ ms$^{-1})$	v $(10^{-3}$ ms$^{-1})$	v $(10^{-3}$ ms$^{-1})$	u $(10^{-6}$ ms$^{-1})$	v $(10^{-5}$ ms$^{-1})$
80	2·54605	3·84677	4·86971	−5·58589	−2·05654
120	2·54614	3·84938	4·86927	−5·58662	−2·06597
160	2·54619	3·85066	4·86906	−5·58697	−2·07075
240	2·54623	3·85191	4·86886	−5·58730	−2·07561
320	2·54625	3·85251	4·86876	−5·58746	−2·07810

As an example of the convergence behaviour of our computations in the interior of the problem area, some velocity components are computed in a number of points with an increasing truncation number. Figure 4 shows the chosen points. In this calculation, all etch-hole parameters are equal to unity. The results of these computations are given in Table 1. We can conclude that the series do converge for the interior points (points 1–4). In contrast the series converge only very slowly for point 5. This difference in convergence behaviour can be explained by considering the mathematical form of the series. In the interior points the argument of the exponent is negative, which leads to a rapid decrease for increasing k. On the other hand, at the region interfaces the argument of the exponent is equal to zero, which makes the convergence behaviour much slower. The convergence of the series in the interior points can even be improved by methods described in the second part of this section.

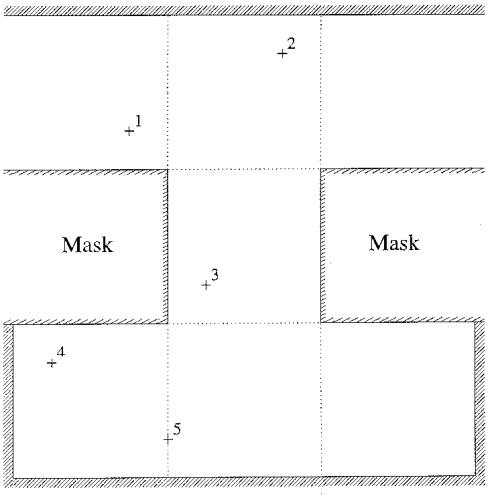

Figure 4. The points (1–5) where a velocity component is computed.

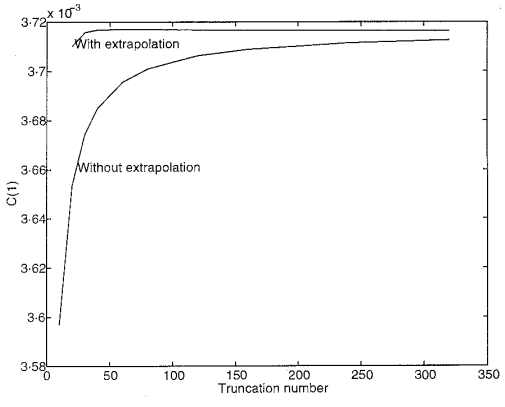

Figure 5. Coefficient $C_1^{(N)}$ as a function of the truncation number, without and with Richardson extrapolation.

The second source of inaccuracies we consider is the inaccuracy caused by the truncation of the infinite linear systems. The truncation of the linear systems has two effects: the remaining parts of the series are neglected, and due to the truncation the coefficients that are computed

Table 2. Convergence behaviour of velocities at arbitrary points computed with the Richardson extrapolation method for the coefficients as functions of the truncation number N.

	Point 1	Point 2	Point 3	Point 4	Point 5
N	u (10^{-1} ms^{-1})	v (10^{-3} ms^{-1})	v (10^{-3} ms^{-1})	u (10^{-6} ms^{-1})	v (10^{-5} ms^{-1})
80	2·54632	3·85461	4·86840	−5·58809	−2·04813
120	2·54632	3·85449	4·86843	−5·58801	−2·06103
160	2·54631	3·85440	4·86845	−5·58796	−2·06793
240	2·54631	3·85434	4·86846	−5·58793	−2·07405

Table 3. Final values for the velocities computed with the help of both extrapolation methods.

	Point 1	Point 2	Point 3	Point 4	Point 5
N	u (10^{-1} ms^{-1})	v (10^{-3} ms^{-1})	v (10^{-3} ms^{-1})	u (10^{-6} ms^{-1})	v (10^{-5} ms^{-1})
1000	2·546310	3·854340	4·868463	−5·587932	−2·077489

contain an error. We start with a consideration of the inaccuracy of the coefficients. In Figure 5 we can see the coefficient $C_1^{(N)}$ as a function of the truncation number N. It can be seen from this Figure that

$$C_1^{(N)} = C_1^{(\infty)} + \alpha/N + o(1/N). \tag{7.2}$$

This information can be used to obtain more accurate results by an application of Richardson's extrapolation method. The second line in Figure 5 gives the results of this extrapolation as a function of the truncation number N and from this example it is clear that the values of the coefficients are improved by this extrapolation. The higher-order terms in expansion (7.2) cannot easily be removed, since the leading term is not polynomial in $1/N$. This extrapolation method is applied to compute the velocities in the same points as in Table 1. From Table 2 it can be concluded that the convergence for the interior points is better after application of Richardson's extrapolation. However, the convergence in the point at the interface does not improve. Next we consider the neglected remaining part of the infinite series. In Figure 6 the extrapolated coefficients C_k are plotted logarithmically as a function of the coefficient index k. This Figure gives reason to assume that the coefficients contain some asymptotic behaviour of the form

$$C_k = \alpha * k^{-\beta}. \tag{7.3}$$

While the first C_k values do not show this asymptotic behaviour, and the last terms are affected by the truncation of the series, we use the coefficients from $k = 10$ to $k = 100$ for extrapolation of the C_k values with the help of (7.3) to approximate C_k for large k. In our case, the value of β varies from 1·4 to 1·7.

With the help of this second extrapolation method, the velocities are computed again. In Table 3 the values of the velocities at the points chosen in Figure 4 and computed with the help of both extrapolation methods are given. From this Table it can be concluded, that the values in the interior of the subregions are improved by the use of both extrapolation methods.

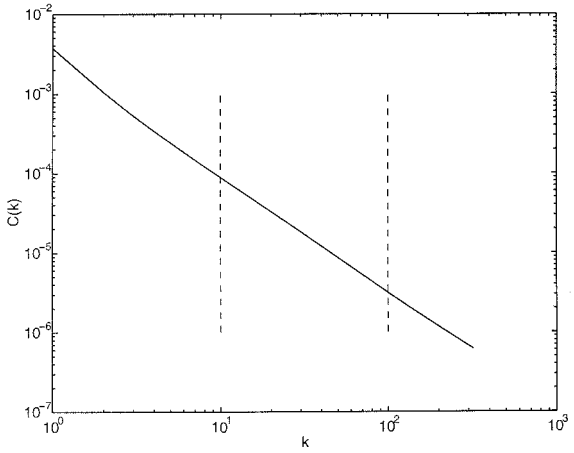

Figure 6. Logarithmic plot of the (Richardson) extrapolated coefficients C_k as a function of k.

However, these extrapolation methods do not improve the accuracy of the computations on the region interfaces (point 5 in our examples).

Although the coefficients in the eigenfunction expansion converge slowly, the solution can be calculated accurately in the interior of the sub-domains after application of the two extrapolation techniques. Therefore, the results obtained can be used to validate other numerical methods for Stokes flow.

8. Results

In this section we compute the stream function for different flow geometries with the help of both extrapolation methods.

In an etching situation the upper plate is absent. To simulate this the distance from the upper plate to the etch hole (D/W) is chosen equal to 20. With this distance fixed, we can vary the etch-hole parameters $(g/W, f/W$ and $d/W)$.

The first configuration we present (Figure 7) is a contour plot of the stream function with $g/W = 0{\cdot}1, f/W = 1{\cdot}0$ and $d/W = 1{\cdot}0$. In this picture we see one vortex in the central region of the hole, and two vortices at the left and right-hand sides of the etch hole. The stream function in these last two vortices is very small in comparison with the stream function in the central vortex. This indicates that there is almost no fluid flow at the left and right-hand sides of the etch hole. Since etching is dependent on the transport of the dissolved metal, the etching process on the vertical boundaries of the etch hole proceeds very slowly in comparison with etching in the downward direction for this particular geometry.

As a second example we consider a geometry with a relative thick mask in comparison with the width W of the etch pattern. Figure 8 shows that two vortices arise between the mask edges. The stream function indicates that there is almost no fluid flow in the etched cavity. We can conclude that a relative thick mask decelerates the etching process.

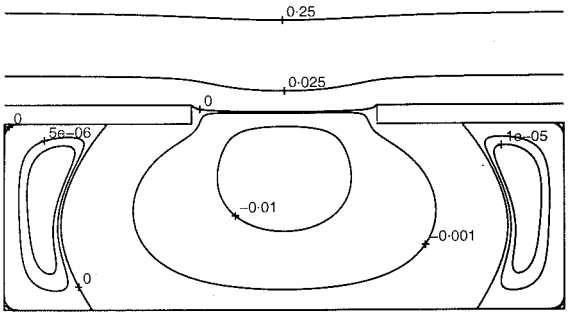

Figure 7. Contour plots for given values of the stream function for an etched hole with $g/W = 0{\cdot}1, d/W = 1{\cdot}0$ and $f/W = 1{\cdot}0$.

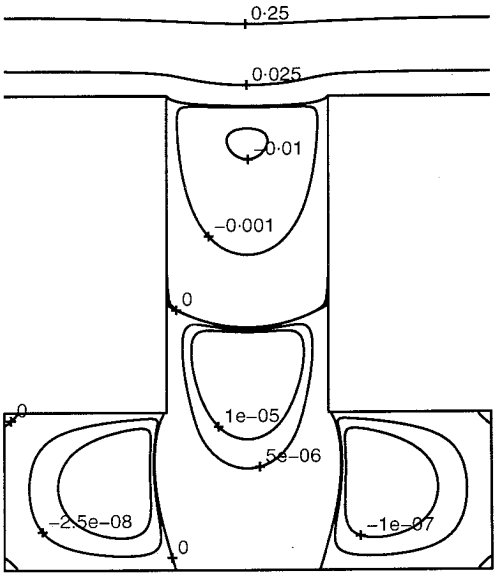

Figure 8. Contour plots for given values of the stream function for an etched hole with $g/W = 2{\cdot}0, d/W = 1{\cdot}0$ and $f/W = 1{\cdot}0$.

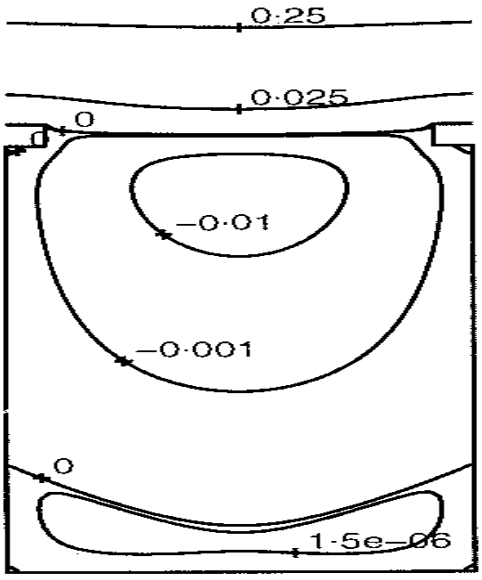

Figure 9. Contour plots for given values of the stream function for an etched hole with $g/W = 0{\cdot}1, d/W = 2{\cdot}0$ and $f/W = 0{\cdot}1$.

What can also be seen from this picture, is that the side eddies do not quite extend to the reentrant corner, a property already shown by Takematsu [1]. The flow field near the corners of the geometry is dominated by the singularity solutions (7.1). While the solutions are considered in a small region around a corner, only the first terms have to be taken into account. These terms do not become zero in this region except on the walls; these functions do not have a dividing streamline.

When the depth-width ratio of the etched hole is increased (see Figure 9) we see two vortices in the hole. The stream-function values show that the fluid flow is negligible in the lowest vortex. Hence the etching in the vertical direction is much slower than in the horizontal direction.

From Figure 7 and 9 it can be concluded that the most appropriate rectangular approximation of a natural etching geometry looks like the one shown in Figure 10. If the width is larger than the height the reduced etching in the horizontal direction results in a relatively

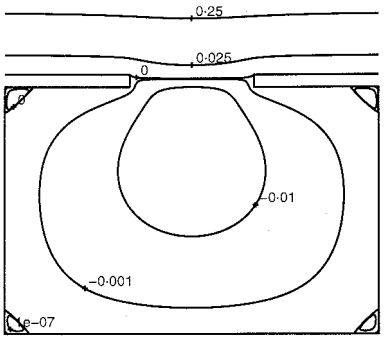

Figure 10. Contour plots for given values of the stream function for an etched hole with $g/W = 0{\cdot}1$, $d/W = 2{\cdot}0$ and $f/W = 1{\cdot}0$.

deeper etch hole and vice versa. In the geometry in Figure 10 there is only one central vortex which implies that the etch rate will be approximately the same for the vertical and horizontal directions.

Summarising, the method used can be applied to rectangular etch-hole geometries and gives satisfying results for the stream function and the stream velocities. The truncation of the infinite series causes inaccuracies. These inaccuracies can be cured by two extrapolation methods. However, the most important sources of inaccuracy in the answers are the singularities on the mask-edge corners. It is possible to solve this problem by adding the leading singular terms to the series expansion, as in the work of Kelmanson [27] and the work of Bohou [28] on the boundary-element method. This is beyond the scope of this paper and will be a subject for future research.

Acknowledgements

This work was supported by STW, the Netherlands Technology Foundation, under project TW144.3286. The authors wish to thank Dr. D. Dijkstra, Professor H. K. Kuiken and Prof. P. J. Zandbergen for stimulating discussions and recommendations.

References

1. M. Takematsu, Slow viscous flow past a cavity. *J. Phys. Soc. Japan* 21 (1966) 1816–1821.
2. R. E. Chilcott, A review of separated and re-attaching flows with heat transfer. *Int. J. Heat Mass Transfer* 10 (1967) 783–797.
3. T. C. Reiman and R. H. Sabersky, Laminar flow over rectangular cavities. *Int. J. Heat Mass Transfer* 11 (1968) 1083–1085.
4. V. O'Brien, Closed streamlines associated with channel flow over a cavity. *Phys. Fluids* 15 (1972) 2089–2097.
5. J. F. Stevenson, Flow in a tube with circumferential wall cavity. *J. Appl. Mech.* 40 (1973) 355–361.
6. H. K. Kuiken, Heat or mass transfer from an open cavity. *J. Eng. Math.* 40 (1978) 129–155.
7. H. K. Kuiken and R. P. Tijburg, Centrifugal etching: a promising new tool to achieve deep etching results. *J. Elchem. Soc.* 130 (1983) 1722–1729.
8. M. J. Lighthill, Contributions to the theory of heat transfer through a laminar boundary layer. *Proc. R. Soc. London* A202 (1950) 359–377.
9. D. D. Joseph and L. Sturges, The free surface on a liquid filling a trench heated from its side. *J. Fluid Mech.* 69 (1975) 565–589.
10. D. D. Joseph, The convergence of biorthogonal series for biharmonic and Stokes flow problems, part I. *SIAM J. Appl. Math.* 33 (1977) 337–347.

11. D. D. Joseph and L. Sturges, The convergence of biorthogonal series for biharmonic and Stokes flow edge problems, part II. *SIAM J. Appl. Math.* 34 (1978) 7–26.
12. S. A. Trogdon and D. D. Joseph, Matched eigenfunction expansions for slow flow over a slot. *J. Non-Newt. Fluid Mech.* 10 (1982) 185–213.
13. R. C. Alkire, H. Deligianni and J.-B. Ju, Effect of fluid flow on convective transport in small cavities. *J. Elchem. Soc.* 137 (1990) 818–824.
14. J. N. Harb and R. C. Alkire, Transport and reaction during pitting corrosion of Ni in 0.5M NaCl. *J. Elchem. Soc.* 138 (1991) 3568–3575.
15. M. Georgiadou and R. C. Alkire, Anisotropic chemical pattern etching of copper foil. III Mathematical model. *J. Elchem. Soc.* 141 (1994) 679–689.
16. C. B. Shin and D. J. Economou, Effect of transport and reaction on the shape evolution of cavities during wet chemical etching. *J. Elchem. Soc.* 136 (1989) 1997–2004.
17. C. B. Shin and D. J. Economou, Forced and natural convection effects on the shape evolution of cavities during wet chemical etching. *J. Elchem. Soc.* 138 (1991) 527–538.
18. K. G. Jordan and C. W. Tobias, Simulation of the role of convection in electro deposition into microscopic trenches. *J. Elchem. Soc.* 138 (1991) 1933–1939.
19. J. M. Occhialini and J. J. L. Higdon, Convective mass transport from rectangular cavities in viscous flow. *J. Elchem. Soc.* 139 (1992) 2845–2855.
20. J. Fadle, Die Selbstspannungs-Eigenwertfunktionen der quadratischen Scheibe. *Ing. Arch.* 11 (1941) 125–148.
21. P. F. Papkovich, Über eine form der Lösung des Byharmonischen Problems für das Rechteck. *C. r. (Dokl.) Acad. Sci. URSS* 27 (1970) 334–338.
22. C. I. Robbins and R. C. T. Smith, A table of roots of sin $z = -z$. *Phil. Mag.* (7) 39 (1948) 1005.
23. R. C. T. Smith, The bending of a semi-infinite strip. *Austral. J. Sci. Res.* 5 (1952) 227.
24. H. K. Moffatt, Viscous and resistive eddies near a sharp corner. *J. Fluid. Mech.* 18 (1964) 1–18.
25. Personal communication.
26. R. W. de Vries and P. J. Zandbergen, The numerical solution of the biharmonic equation, using a spectral multigrid method, in W. F. Ballhaus and M. Y. Hussaini, (eds.), *Advances in Fluid Dynamics; proc. of the symposium in honor of Maurice Holt on his 70th birthday* (1989) 25–35.
27. M. A. Kelmanson, Modified integral equation solution of viscous flows near sharp corners. *Computers and Fluids* 11, No. 4 (1983) 307–324.
28. X. Bohou, Some problems in slow viscous flow. Report S 29, The Danish Center for Applied Mathematics and Mechanics, (1985).